Experiments in Fluids (2024) 65:54
https://doi.org/10.1007/s00348-024-03791-3

RESEARCH ARTICLE

Spatially resolved measurement of the electrostatic charge of turbulent powder flows

Wenchao Xu[1] · Simon Jantač[1] · Tatsushi Matsuyama[2] · Holger Grosshans[1,3]

Received: 12 June 2023 / Revised: 21 February 2024 / Accepted: 22 February 2024 / Published online: 25 March 2024

Abstract
This article reports on measurements of the electrostatic charge of particles in a turbulent duct flow. In contrast to previous charge measurements, which do not apply to turbulent flows or give only the sum of all particles' charges, the new method resolves the charge of a turbulent powder flow spatially. The experiment consists of a particle tracking velocimetry (PTV) system and electrode plates that generate an electric field. By comparing particle velocities and accelerations with and without the electric field, the time-averaged local particle charge profile is derived. Spatially resolving the charge profiles unveiled bipolar particle flow. The average of the charge profiles agreed well with a conventional Faraday pail measurement, demonstrating the accuracy of our measurements. However, the peak value of the charge profiles was 76 times higher than the average of the particles' charge.

1 Introduction

In the UK and Germany, undetected static electricity causes one dust explosion every ten days (Glor 2003). Out of all industrial powder operations, pneumatic conveying by turbulent duct and pipe flows leads by far to the highest charge (Klinzing 2018). Even though the understanding of powder flow charging in pneumatic conveyors was extensively progressed by Faraday pails (Ndama et al 2011; Peltonen et al 2018; Xu and Grosshans 2023), they cannot spatially resolve the charge. Therefore, local charge peaks of both polarities remained hidden.

Further, simulations of powder flow charging remain immature due to a lack of detailed validation data (see the review of Grosshans and Jantač 2023). Direct numerical simulations nowadays resolve the powder charge profiles in ducts, pipes, and channels (Grosshans and Papalexandris 2017; Zhang et al 2023). These spatially highly resolved simulations revealed the small-scale mechanisms determining the powder flows' charging rate. For example, particle-bound charge transport led to vigorous charging of highly inertial particles and inter-particle charge diffusion to the charging of low inertial particles. The validation and improvement of these codes urgently require spatially resolved experiments.

Powder flows charge when particles contact surfaces or other particles, or without contact, for example, by absorbing ions from the atmosphere (Gouveia and Galembeck 2009). When a Faraday pail encloses the flow, the charge of the particles inside the pail induces an equal charge on its conductive surface. The induced charge can be displayed by an electrometer. The Faraday pail gives the algebraic sum of the enclosed particles' charge or their average charge if the number of particles is known.

The Faraday pail's advantage is its simplicity and price; its disadvantage is that it may detect only a minute fraction of the total charge. For example, through contact with other particles of the same material, powder charges

✉ Holger Grosshans
holger.grosshans@ptb.de

Wenchao Xu
wenchao.xu@ptb.de

Simon Jantač
simon.jantac@ptb.de

Tatsushi Matsuyama
tatsushi@t.soka.ac.jp

[1] Analysis and Simulation in Explosion Protection, Physikalisch-Technische Bundesanstalt (PTB), Bundesallee 100, Braunschweig 38116, Germany

[2] Faculty of Engineering, Soka University, Hachioji 192-8577, Japan

[3] Institute of Apparatus and Environmental Technology, Otto von Guericke University of Magdeburg, Universitätsplatz 2, Magdeburg 39106, Germany

bipolar (Waitukaitis et al 2014; Konopka and Kosek 2017). A bipolar powder comprises particles of both polarities, while their overall charge can remain neutral. In a turbulent flow, mid-sized particles obtain the highest negative and large ones the highest positive charge (Jantac and Grosshans 2024). If the powder within the Faraday pail's measurement volume is bipolar, the detected charge may be close to zero.

For the same reason, a Faraday pail cannot resolve particle charge distributions, spatial charge profiles, or any other detailed quantity. Thus, local charge peaks and their possible discharges continue to threaten process safety.

Alternatively, when the conveying pipe is grounded, the charge transferred from the particles to the wall can be detected as electric current (Matsusaka and Masuda 2006; Taghavivand et al 2020). Likewise, this signal represents the sum of the charge without any further resolution.

A different flow charge measurement technology applies an external electric field to the powder. The field separates particles of different polarity (Toth et al 2017) or deflects the particle trajectories (Mazumder et al 1991; Hammond et al 2019). From the balance of forces acting on the individual particles, the deflected trajectories tell the particles' charge.

The problem of those force balance methods is that they do not apply to turbulent flows. Solving the force balance requires the knowledge of the flow velocity at the location of the particles, which is readily available in a vacuum, still fluid, or laminar flow. In turbulence, chaotic fluid forces affect the particles' trajectories. Thus, the trajectories do not tell the particles' charge or polarity.

The simultaneous measurement of the particles' trajectories and the turbulent flow velocity requires seeding the fluid with tracers. Seeding tracers to the flow is usually impractical in industrial conveying systems since it interrupts the operation and contaminates the product.

Another force balance approach uses a periodically oscillating electric field. From the oscillation amplitude of a responding particle, its charge can be deduced. This technique has been applied to free-falling cloud droplets of a size of 10 µm to 100 µm (Twomey 1956; Takahashi 1973; Wells and Gerke 1919). The droplets fall through quiescent air, which enables solving the force balance. However, the lack of fluid forces prevents applying the method to turbulent flows. Thus, today's force balance approaches do not apply to turbulent flows where the fluid forces on the particles are unknown.

Induction probes mounted at towers resolved the internal electrification of dust storms (Zhang and Zhou 2020), but scaling down the probes to industrial flows would heavily intrude on the hydrodynamics. Therefore, in fluidized beds, induction probes spatially resolved the charge profile at the boundary walls (Gajewski 1985), while the charge within the flow is unknown.

A methodology to measure the charge profile of powder conveyed in turbulent duct, pipe, and channel flows is unavailable today. Consequently, state-of-the-art experimental data are limited to reveal global trends, e.g., the relation between the flow velocity, solid mass loading, or particle material with the total powder charge. Local charge peaks remain undetected by current measurement technology. Moreover, bipolar charging of same-material particles was found in vacuum (Waitukaitis et al 2014), but due to the lack of a measurement method, not in turbulent flow. This lack hinders safety evaluations, particularly of pneumatic conveyors, and the validation of simulations.

To measure the powder charge profiles in a turbulent duct flow, we invented and patented an in situ, laser-based measurement technology (Grosshans 2022). This new technology can spatially resolve the time-averaged particle charge profile, including flow regions of opposite polarities. In this paper, we communicate the realization of the technology in our lab and the first successful measurements.

2 Experimental method

2.1 Test-rig and measurement section

For developing the measurement technology, we installed a pneumatic conveying pilot plant (Fig. 1a) in our laboratory. A mini screw feeder manufactured by SEIWA GIKEN supplies particles to the duct's top. The duct conveys the powder vertically downward, aligned with the gravitational acceleration. After the duct's outlet, a cyclone and a filter separate the particles from the airflow. A blower sucks the air and powder through the duct, cyclone, and filter. Between the blower and the filter, an orifice airflow meter O-METER type OM4S measures the airflow rate.

A conventional Faraday pail provides validation data for the new measurement method. The pail encloses the cyclone and the filter, while their metallic housings are connected to a Keithley 6514 electrometer. Thus, the electrometer measures the sum of the charge of the particles collected by the cyclone and the filter.

The duct is made of transparent PMMA (polymethyl methacrylate), providing optical access for particle tracking velocimetry (PTV) (Fig. 1b and c). To avoid the laser beam's diffraction at curved surfaces, the duct is of a square cross-section. Each planar wall's inner side length is $D = 50$ mm, and its thickness is 0.16 D. The duct's length, from the inlet to the beginning of the measurement section, is 33 D. The flow in the duct is statistically stationary.

In the measurement section, at opposite duct walls, two parallel electrodes connected to a high-voltage power supply generate an electric field. To avoid contact with the particles, the electrodes are attached to the outside of the

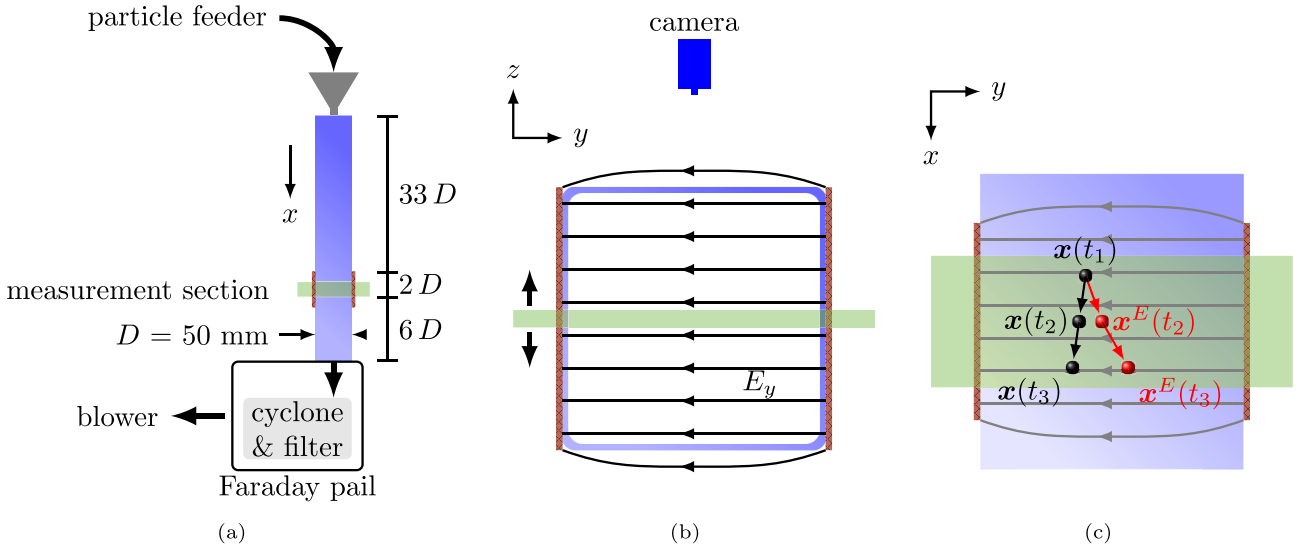

Fig. 1 (**a**) Pneumatic conveying pilot plant to test the new measurement system. (**b**) Components of the measurement system: electric field (E_y), traversable laser sheet (green), and PTV camera. (**c**) Motion of a particle from $\boldsymbol{x}(t_1)$ with the E-field to $\boldsymbol{x}^E(t_3)$ and without the E-field to $\boldsymbol{x}(t_3)$

duct. They are manufactured of thin, transparent Indium-Tin-Oxide (ITO) coated plastic films that let the laser beam pass through. The negatively charged electrode is located at $y/D = -0.16$ and the positive one at $y/D = 1.16$. The enclosed PMMA duct distorts the electric field. Figure 2 shows the y component of the electric field computed with COMSOL.

The electric field can be switched on or off. When the electric field is switched on, it accelerates positively charged particles in the $-y$ and negatively charged particles in the $+y$ direction. The measurement system analyzes the particles' response to the electric field.

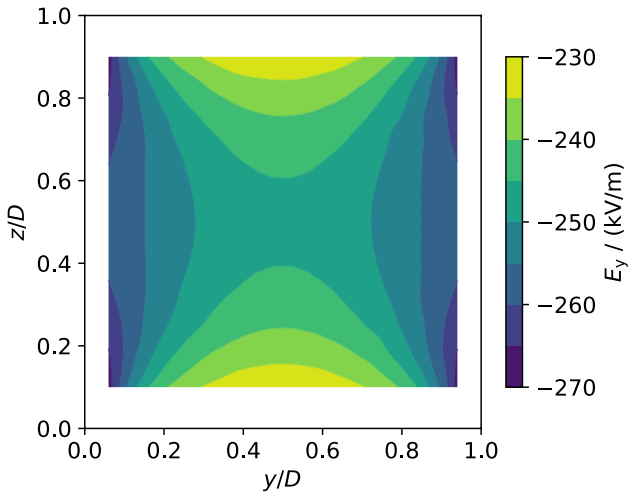

Fig. 2 Distortion of the electric field in y direction by the PMMA duct, computed with COMSOL

A 40-W pulse diode (LD-PS) laser illuminates the flow at a wavelength of 450 nm ± 20 nm. The laser emits repetitive pulses, each lasting 34.5 µs, at a frequency of 4353 s^{-1}.

The laser beam points in y direction. Lenses shape the beam into a sheet that spreads across the x–y plane. In the z direction, the laser's intensity profile has an effective thickness of about 2 mm along the whole camera field of view. In the streamwise direction (x), the sheet begins D after the edge of the electric field spans D downstream. To scan the complete cross-section of the duct, the laser sheet is traversable in the z direction (see Fig. 1b).

The gas flow's bulk Reynolds number was 13 200, based on D and the average velocity. The particles were monodisperse, spherical, of a size of $d = 100$ µm, and made of PMMA. According to the manufacturer, the standard deviation of the particle size was less than 3.5 µm. The powder mass flow rate was 0.2 g/s ± 0.02 g/s, corresponding to an average particle number density of about 3.3×10^7 m^{-3}, solid volume fraction of 1.7×10^{-5}, or mass fraction of 1.7×10^{-2}. The relative humidity and temperature in the laboratory during the tests were 47% and 19.5 °C.

2.2 PTV setup

A 2D2C particle tracking velocimetry (PTV) system captured the particles' motion within the measurement section. Part of the PTV system is a Chronos 2.1 monochrome high-speed camera operating at a frame rate of 4352 fps. At the applied frame rate, the camera has a resolution of 800 × 600 pixels, each pixel of a size of 100 µm × 100 µm. At this resolution and frame rate, the camera's internal memory allows a

maximum recording duration of 10.94 s, yielding a total of 47 610 frames. Thus, the data presented in this paper were averaged over 47 609 time intervals.

For initial image processing, a filter based on proper orthogonal decomposition (POD) eliminated static background elements (Mendez et al 2017). This filter removes bright artifacts, such as the duct's illuminated sidewall and reflections of contaminations on the inner wall, thus mitigating errors in the near-wall area of the images.

To extract particle trajectories, the PTV system identifies and links image features using the open-source Python package Trackpy (Allan et al 2023). Trackpy is based on the tracking algorithm by Crocker and Grier (1996). Further, it achieves sub-pixel precision through the least-squares fitting method (van der Wel and Kraft 2017).

Since the method described below to derive the particle charge requires precise acceleration data, we stringently filtered spurious trajectories. The filter retains only particle trajectories identified on at least seven subsequent frames and discards any trajectory on fewer frames. Those trajectories that met this criterion were further refined by a B-spline smoothing filter (Eilers and Marx 1996) that removes irregularities from the data. Also, the filter rejected the trajectories for which the residuals of the smoothing were above a threshold (see section 3).

2.3 Deriving *Q* from the force balance

The force balance of a charged particle in an electric field in y direction, the longitudinal axis of the laser beam reads

$$m a_y^E = F_{\mathrm{d},y} + F_{\mathrm{c},y} + F_{\mathrm{e},y}\,, \tag{1}$$

where m and a_y^E are the particle's mass and wall-normal acceleration. The right-hand side of the above equation sums the forces acting on the particle, the drag force, $F_{\mathrm{d},y}$, collisional force, $F_{\mathrm{c},y}$, and electrostatic force, $F_{\mathrm{e},y}$. The collisional force term includes the forces on a particle during contact with a duct wall or other particles. Gravitational forces vanish since the laser points horizontally.

The drag term in y direction is

$$F_{\mathrm{d},y} = m\frac{u_{\mathrm{g},y} - u_y^E}{\tau}\,, \tag{2}$$

where $u_{\mathrm{g},y}$ is the free-stream velocity of the gas surrounding the particle and u_y^E the particle's velocity. Assuming a Stokes flow, the response time,

$$\tau = \rho\, d^2/(18\,\mu)\,, \tag{3}$$

is constant. Herein, $\rho = 1150$ kg m^{-3} is the particles' material density and $\mu = 1.825 \times 10^{-5}$ N m^{-2} the dynamic gas viscosity. The Stokes flow assumption is valid for a particle Reynolds number of $Re_{\mathrm{p}} = u_{\mathrm{rel}}\, d/\nu < 1$, where u_{rel} the magnitude of the relative velocity of the particle and the surrounding air, and $\nu = 1.516 \times 10^{-5}$ m^2 s the kinematic gas viscosity.

The electrostatic force,

$$F_{\mathrm{e},y} = Q\big(E_y + E_{\mathrm{oth},y}\big)\,, \tag{4}$$

depends on the particle's charge, Q, and the electric field's component in y direction. The total electric field in the measurement section comprises E_y, generated by the electrodes, and $E_{\mathrm{oth},y}$, the sum of other electric fields, for example, by surrounding charged particles, charge located at the duct walls, or mirror charges.

Substituting Eqs. (2) and (4) in (1) and dividing by the particle's mass yields

$$a_y^E = \frac{u_{\mathrm{g},y} - u_y^E}{\tau} + f_{\mathrm{c},y} + \frac{Q\big(E_y + E_{\mathrm{oth},y}\big)}{m}\,. \tag{5}$$

Out of the terms of this equation, E_y is known, m_{p} is known since the particles are monodisperse, τ is approximated by the Stokes assumption, and a_y^E and u_y^E are measured by PTV.

However, the problem of Eq. (5) lies in the unknown terms $f_{\mathrm{c},y}$, $E_{\mathrm{oth},y}$, and $u_{\mathrm{g},y}$. The instantaneous gas velocity is relevant in turbulent flows with particles of $\tau \ll \infty$, but measuring it simultaneously to the particle velocities requires an additional measurement system and seeding tracer particles, which is impossible in most industrial flows. The collisional force is unknown. Even though it is generally small in dilute flows, it can be locally large. In the following, we propose a solution to this problem based on averaging.

Time averaging Eq. (5) yields

$$\bar{a}_y^E = \frac{\bar{u}_{\mathrm{g},y} - \bar{u}_y^E}{\tau} + \bar{f}_{\mathrm{c},y} + \frac{\bar{Q}E_y + \overline{QE}_{\mathrm{oth},y}}{m}\,. \tag{6}$$

The operator $\bar{\phi}$ denotes the time average over many particles or the electric field at fixed points in space. In other words, $\bar{Q}$ is the spatially resolved profile of the arithmetic mean of the local charge distribution,

$$\bar{Q} = \bar{Q}(\boldsymbol{x}) = \frac{1}{N(\boldsymbol{x})}\sum_{n=1}^{N(\boldsymbol{x})} Q_n(\boldsymbol{x})\,, \tag{7}$$

where N is the number of particles holding a charge Q_n and passing the location $\boldsymbol{x}$ during the measurement.

In an experiment with de-activated electric field, Eq. (6) reduces to

$$\bar{a}_y = \frac{\bar{u}_{\mathrm{g},y} - \bar{u}_y}{\tau} + \bar{f}_{\mathrm{c},y} + \frac{\overline{QE}_{\mathrm{oth},y}}{m}\,, \tag{8}$$

where $\bar{u}_y$ and $\bar{a}_y$ are the particles' velocity and acceleration without the electric field. If $\bar{u}_y^E$ and $\bar{a}_y^E$ are measured shortly after the particles reach the electric field, the field only slightly affects the particle positions. Then, in Eqs. (6) and (8) the terms $\bar{f}_{c,y}$ and $\overline{QE}_{oth,y}$ are equal. Also, because the flow is statistically stationary, the terms $\bar{u}_{g,y}$ are equal. Thus, substracting Eq. (8) from Eq. (6) and solving for $\bar{Q}$ results in

$$\bar{Q} = \left(\bar{a}_y^E - \bar{a}_y + \frac{\bar{u}_y^E - \bar{u}_y}{\tau} \right) \frac{m}{E_y} . \tag{9}$$

In other words, in the above equation, the unknown collisional force, electric field components, and gas phase velocity are eliminated even though being implicitly included, which is the advantage of Eq. (9) over Eq. (5). In return, Eq. (9) provides the time-averaged charge instead of the charge per particle.

3 Accuracy of the method

3.1 PTV algorithm and equipment

In total, 1.8 million recorded particle trajectories passed the PTV algorithm's smoothing filter. The filter's small threshold keeps the quality of the remaining trajectories high; the standard deviation of their residual is 1.9×10^{-3} pixels.

The location of the recorded particles distributes over the duct's entire cross-section. At each location where Eq. (9) was evaluated, u_y^E, u_y, a_y^E, and a_y were averaged over 700 to 5500 measured values. The standard deviation of these values propagates to a standard error of the mean (SEM) of the particle charge between 1.4 fC and 3.2 fC, depending on the location, and an average SEM of 2.0 fC.

The PTV camera detects the particle locations with an uncertainty of approximately 1.6×10^{-3} pixels (Savin and Doyle 2005), less than 0.2% of the average particle displacement between subsequent recorded images. At all locations of the duct's cross-section, this detection error leads to an extremely low SEM of the particle charge ($\ll 0.1$ fC).

According to the manufacturer, the maximum voltage error of the electric field's power supply is 0.5%. This error propagates linearly to a maximum error of the electric field and particle charge according to Eq. (9) of 0.5%.

Further, the uncertainty of the particle diameter (3.5 µm) affects Eq. (9) through the particle mass by the diameter's third-order non-central moment. Thus, the average particle mass is 0.37% higher than the nominal mass that enters the equation, which leads to a negative offset of 0.37% of the derived $\bar{Q}$.

3.2 Stokes flow assumption

The mathematical derivation of Eq. (9) requires the particle response time to be known and constant. We satisfied this requirement by assuming a Stokes flow (Eq. (3)), which is valid for $Re_p < 1$. However, the particles' Reynolds number based on their terminal velocity in still air is approximately 1.5 (Clift et al 1978) and exceeds this value instantaneously in turbulence. Thus, the Stokes flow assumption introduces an error to Eq. (9).

To evaluate the error of the charge of powder in turbulence related to the Stokes flow assumption, we theoretically analyze a single charged particle moving in x direction ($u_x \gg u_y$ and $u_x \gg u_y^E$) through a uniform and constant flow. Analogous to the averaged Eq. (9), the charge of a single particle is, based on Stokes' assumption,

$$Q_{\text{Stokes}} = \left(a_y^E - a_y + \frac{u_y^E - u_y}{\tau} \right) \frac{m}{E_y} . \tag{10}$$

According to Oseen (Batchelor 2010), who included first-order inertial effects, the particle's response time for Reynolds numbers up to 5 decreases to

$$\tau' = \tau \left(1 + \frac{3}{16} Re_p \right)^{-1} . \tag{11}$$

Since the particle moves mainly in the x direction, Re_p and τ' are not affected by the change of the particle's velocity in the y direction. Thus, based on Oseen's correction, the particle's charge is

$$Q_{\text{Oseen}} = \left(a_y^E - a_y + \frac{u_y^E - u_y}{\tau'} \right) \frac{m}{E_y} . \tag{12}$$

The error of the particle's charge due to Stokes assumption, $err_Q = Q_{\text{Stokes}} - Q_{\text{Oseen}}$, is

$$err_Q = \left(\frac{u_y^E - u_y}{\tau} - \frac{u_y^E - u_y}{\tau'} \right) \frac{m}{E_y} . \tag{13}$$

Inserting Eq. (11) into (13) and reordering the terms yields

$$err_Q = \frac{3}{16} \frac{m}{\tau E_y} Re_p \left(u_y - u_y^E \right) . \tag{14}$$

The last term can be estimated by the velocity in y direction a particle reaches in the electric field, $\left(u_y - u_y^E \right) = \delta t^E Q E_y / m$, where $\delta t^E = 2D/u_x$ is the particle's residence time in the measurement section. Using this estimation and dividing Eq. (14) by Q gives the relative error

$$err_{\text{rel},Q} = \frac{3}{16} \frac{\delta t^E}{\tau} Re_p . \tag{15}$$

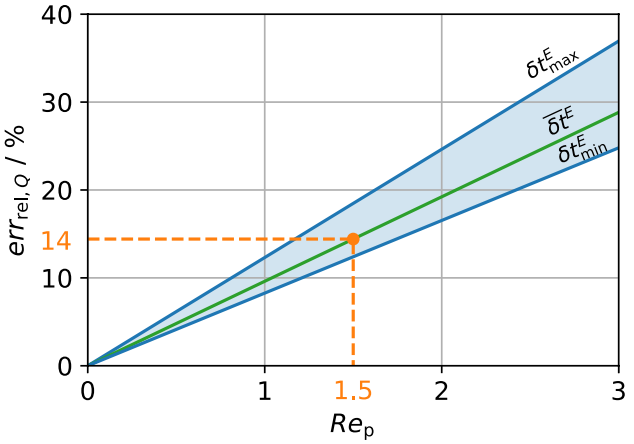

Fig. 3 Relative error of Eq. (9) stemming from the Stokes flow assumption. The green line is for the mean residence time in the measurement section, $\overline{\delta t}^E = 18$ ms. The orange symbol marks $Re_p = 1.5$ based on the particles' settling velocity in still air

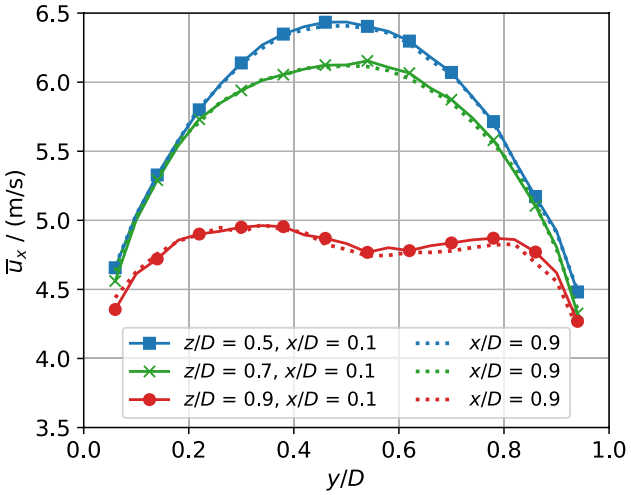

Fig. 4 Time-averaged streamwise particle velocities. Comparison of the profiles at the beginning and end of the laser beam for three different slices averaged over $x/D \pm 0.1$

This expression reveals that for a given τ, i.e., particle diameter, material density, and gas viscosity, the error due to the Stokes flow assumption scales linearly with two factors: the particles' Reynolds number and residence time in the measurement section. While Re_p is a characteristic of the flow, δt^E can be reduced by shortening the measurement section.

Figure 3 plots Eq. (15). The green line represents the mean $\overline{\delta t}^E = 18$ ms determined from the mean downstream velocity, $\bar{u}_x$, of all particles in our experiment. The orange symbol marks the error of 14% based on the particles' settling velocity in still air. Finally, the lines for $\delta t^E_{min} = 15$ ms and $\delta t^E_{max} = 23$ ms depict the error of the particle with the longest and shortest residence time, i.e., the lowest and highest measured u_x.

3.3 Flow and measurement scales

Our experimental procedure requires two measurements while the electric field is switched off and on. To obtain representative average particle velocities and accelerations, the measurements' durations are approximately 840 times the flow time scale $D/\bar{u}_x$.

At the same time, to temporally resolve changes in the mean flow, the complete measurement procedure needs to be short compared to the time scale of boundary condition changes. Since the flow in the test rig is statistically stationary, this condition is fulfilled.

Contrary to averaging in time, the measurements resolve the mean flow changes in space. Thus, there is no limit to the spatial resolution of the method in spanwise (y and z) direction.

In the streamwise direction, the length of the measurement section is a compromise between spatial accuracy and a low signal-to-noise ratio. The signal, the measured velocity and acceleration responses, is the stronger the longer the electric field is.

On the other hand, the measurement section needs to be shorter than the length scale of the changes to the mean flow in the downstream direction. In our test rig, the flow is not yet fully developed when reaching the measurement section. However, Fig. 4 shows that the particles' streamwise velocity profiles do not change from the beginning to the end of the laser beam. Thus, the measurement section is sufficiently short to spatially resolve the flow in the x direction.

Nevertheless, the electric field gives rise to other errors. The stronger the particles react to the electric field, the more invasive the measurement. Analogous to the above estimation of the particles' mean spanwise velocity response, we estimate their mean change of location in y direction due to the electric field to $0.5(\overline{\delta t}^E)^2 Q E_y/m \approx 0.01\,D$ (assuming $Q = 10$ fC). Thus, the measurement was slightly invasive. Moreover, this location change propagates to an uncertainty of the charge profiles' spatial coordinates.

Further, the electric field changes the wall collision frequency. Thus, close to the walls, $\bar{f}_{c,y}$ in Eqs. (6) and (8) differ, which violates the assumptions underlying Eqs. (9). The product of the particles' residence time and measured spanwise velocity implies that they move less than $|y| < 0.03\,D$ within the measurement section. Therefore, in the following, we plot data for $0.04 < y/D < 0.96$, where the results are unaffected by wall collisions.

To sum up, our charge measurements are mainly affected by two errors: The SEM of the particles' velocities and accelerations and the error of the particles' response time.

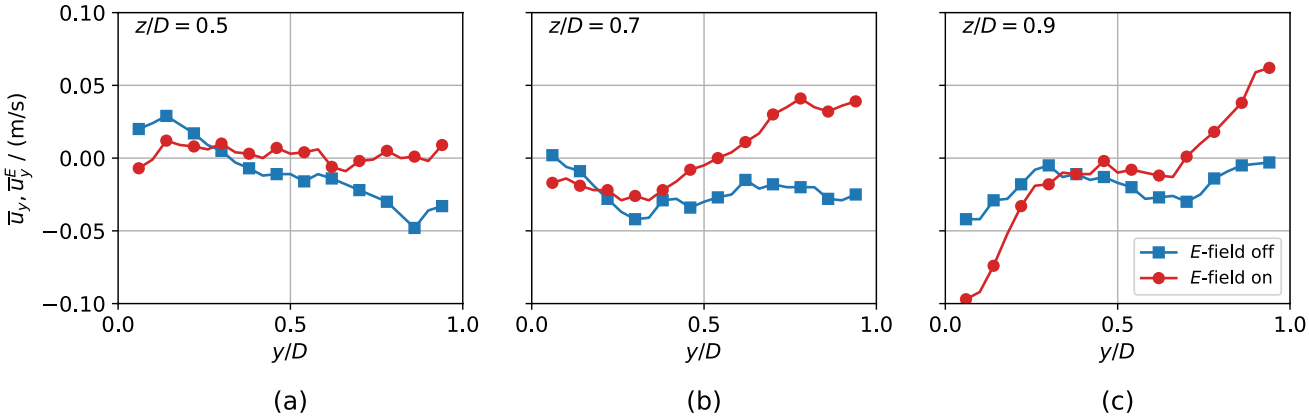

Fig. 5 Time-averaged wall-normal particle velocities responding to the electric field

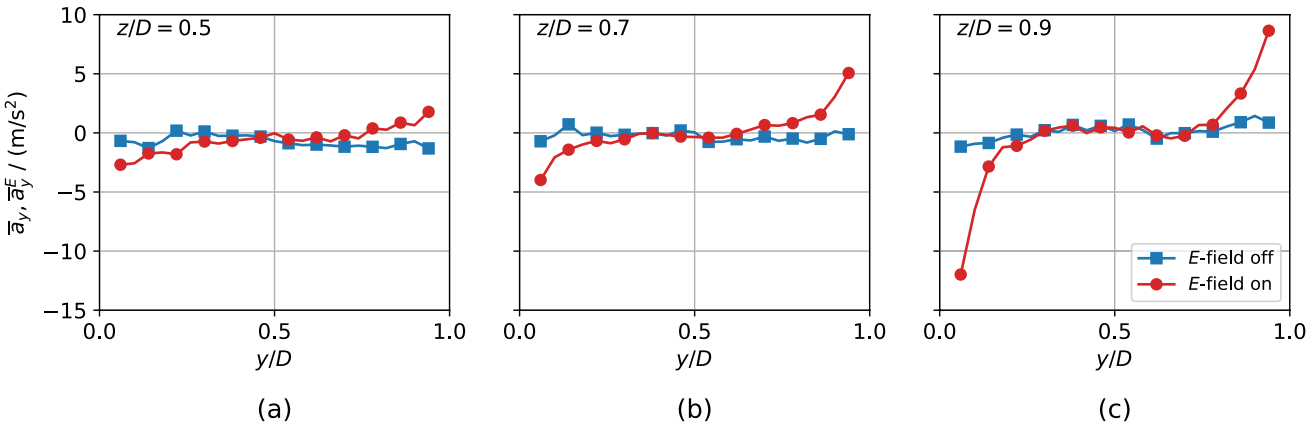

Fig. 6 Time-averaged wall-normal particle accelerations responding to the electric field

Reducing the downstream length of the measurement section can reduce several errors related to spatial uncertainty. However, the chosen distance ensures a low signal-to-noise ratio of the measured velocity and acceleration responses, which we prioritized over spatial accuracy.

4 Spatially resolved particle charge

Figures 5 and 6 present the particles' measured wall-normal velocities and accelerations. All data are time-averaged and depict three spatial profiles in the direction of the electric field. The velocities and accelerations fill the terms on the right-hand side of Eq. (9) to derive the average particle charge presented in Fig. 8.

Downstream of the point-like feeding position at the duct's center, the particle flow widened toward the walls, as reproduced by the nearly symmetric velocity profile in Fig. 5a of the particles without the electric field. When reaching the measurement section, the flow was not yet fully developed (our measurement technique applies to non-developed flows).

In all slices, the particle velocity and acceleration respond to the electric field. The more their profiles differ between the electric field being switched on and off, the more the particles are charged,

In Figs. 5 and 6, the profiles of the slices closest to the wall ($z/D = 0.9$) respond the strongest to the electric field, and the profile of the slice through the duct's centreline ($z/D = 0.5$) responds the least. Also, in each slice, the particles close to the walls at $y/D = 0.0$ and $y/D = 1.0$ respond the strongest.

Figure 7 shows the particle charge over three slices of the duct and Fig. 8 over the duct's cross-section. The shaded areas in Fig. 7 give the two main uncertainties affecting the measurements, resulting from the SEM of the particles' velocities and accelerations and the error of the particles' response time (cf. Sect. 3). We resolved the charge over the entire cross-section by traversing the measurement plane (cf. Fig. 1b) from $z/D = 0.1$ to $z/D = 0.9$ at

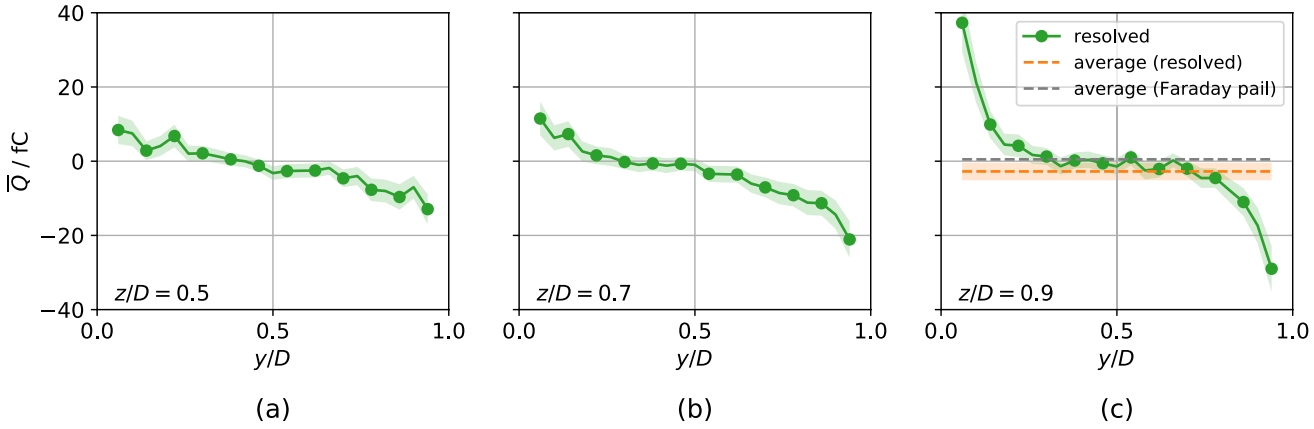

Fig. 7 Spatially resolved time-averaged particle charge over three slices. The average particle charge of the spatially resolved and the Faraday pail measurements agree well

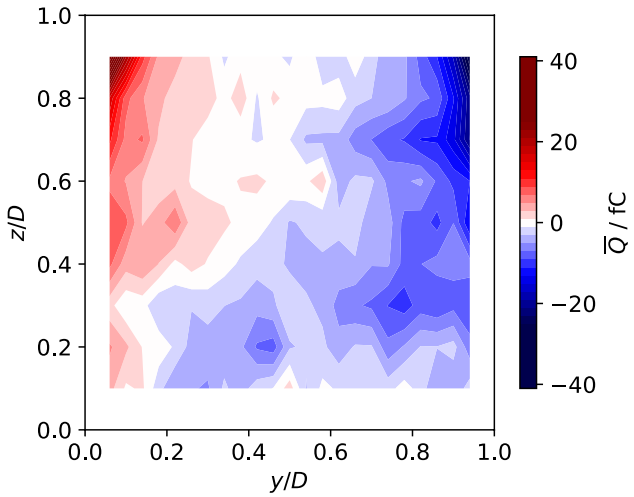

Fig. 8 Spatially resolved time-averaged particle charge over the cross-section

intervals of $z/D = 0.1$, while maintaining the flow conditions, and interpolated between the planes.

It is reiterated that Figs. 7 and 8 depict the time average of the local particle charge profile. Therefore, the sorting of the particles in the electric field also affects the local average charge. The positively charged particles moved in the negative y direction, and the negative ones in the positive y direction.

Figures 7 and 8 reveal a bipolar charged particle flow. The charge profile is nearly symmetric to $y/D = 0.5$. Close to the left wall, the particles carry positive and, close to the right wall, negative charge, while the particles in the bulk are, on average, nearly neutral. The positive and negative charge increase from $z/D = 0.1$ toward $z/D = 0.9$. The positive peak of the charge profile in slice $z/D = 0.9$ is higher in magnitude than the negative peak at the opposite wall of the same slice. However, according to the red and blue areas in Fig. 8, a larger flow region carries an average negative charge.

The measured bipolar charge emanated from same-material contacts with other particles, the feeder, and the duct's walls. During feeding, the particles contacted the feeder's screw, which was already covered with other adhering particles. Since also the duct is made of PMMA, the flow-charged particles underwent only same-material contacts. Same-material contacts, lacking a net direction of charge transfer, resulted in the observed bipolar charging.

Finally, the two horizontal lines in Fig. 7 compare the derived charge to measurements of the Faraday pail (cf. Fig. 1a). During each PTV measurement, we recorded the mass and total charge of the powder captured by the Faraday pail. The gray line in Fig. 7 gives the average charge over the 18 measurements (9 slices, each with and without the electric field) reported in this paper. The standard deviation of the 18 Faraday readings of 0.043 fC is less than the thickness of the gray line. The orange line gives the corresponding average computed from the spatially resolved charge, which means the average of the charge profiles weighted by the local particle concentration. The shaded area indicates the uncertainty of the average resolved charge.

Besides the errors of the spatially resolved measurements discussed in Sect. 3, the duct connecting the measurement section to the Faraday pail contributes to both method's discrepancies. Because of the size of the operating equipment, the Faraday pail starts only 6 D after the end of the measurement section. While the particles traverse through the connecting PMMA duct, they accumulate additional charge that affects the Faraday pail measurement. Additionally, in contrast to the Faraday pail that captures all particles, the spatially resolved measurements miss particles in the wall's proximity.

Within these limits, the averages of the spatially resolved and the Faraday pail measurements agree well. The spatially

resolved measurements result in an average charge of − 2.21 fC, and the Faraday pail measurements in 0.49 fC. Despite the detected charge peaks, both methods return an overall nearly neutral flow.

However, the spatially resolved charge peak is 76 times higher than the average measured by a Faraday pail. Thus, a Faraday pail dramatically underestimates the flow's charge.

5 Conclusions

This paper presents a novel in situ technology for measuring the electrostatic charge of particles in a turbulent duct flow. Unlike existing methods that provide the sum of all particles' charges or are invasive, the developed technology spatially resolves the time-averaged charge profile across the flow. By combining particle tracking velocimetry (PTV) and electrode plates generating an electric field, the local particle charge is derived by comparing particle velocities and accelerations with and without the electric field. We discuss the limitations of the new technique and compare the average derived from the spatially resolved charge profile to the average charge provided by a Faraday pail. Both methods agree well and indicate an overall nearly neutral flow.

However, the spatially resolved results revealed a bipolar particle flow pattern. The resolved charge peak was 76 times higher than the average particle charge detected by the Faraday pail. The presented method opens up a new way to detect so far hidden charge peaks in powder operations and, thus, to enhance industrial safety. Further, it provides the data required to validate and improve current simulations of powder flow charging.

The accuracy analysis points toward the future improvement of the new technique by reducing the length of the electric field.

Author's contribution WX developed the measurement system, with the help of SJ, based on the idea of HG. WX conducted and post-processed all experiments. TM contributed to designing the test rig. HG wrote the first draft of the manuscript. All authors analyzed and interpreted the data, revised the article, and approved the submission.

Funding Open Access funding enabled and organized by Projekt DEAL. W.X., S.J., and H.G. have received funding from the European Research Council (ERC) under the European Union's Horizon 2020 research and innovation program (grant agreement No. 947606 PowFEct).

Data availability Raw and derived data supporting the findings of this study are available from the corresponding author upon reasonable request.

Declarations

Conflict of interest The authors declare that they have no Conflict of interest, or other interests that might be perceived to influence the results and/or discussion reported in this paper.

Ethical approval No studies on humans or animals were part of this work.

References

Allan DB, Caswell T, Keim NC, et al (2023) soft-matter/trackpy: v0.6.1. 10.5281/zenodo.7670439

Batchelor GK (2010) An introduction to fluid dynamics, 14th edn. Press, Cambridge, Cambridge Mathematical Library, Cambridge Univ

Clift R, Grace JR, Weber ME (1978) Bubbles, drops, and particles, 1st edn. Academic Press Inc, New York

Crocker JC, Grier DG (1996) Methods of digital video microscopy for colloidal studies. J Colloid Interface Sci 179(1):298–310. https://doi.org/10.1006/jcis.1996.0217

Eilers PHC, Marx BD (1996) Flexible smoothing with B-splines and penalties. Stat Sci 11(2). 10.1214/ss/1038425655

Gajewski JB (1985) Investigation of the electrification of polypropylene particles during the fluidization process. J Electrostat 17:289–298. https://doi.org/10.1016/0304-3886(85)90029-4

Glor M (2003) Ignition hazard due to static electricity in particulate processes. Powder Technol 135–136:223–233. https://doi.org/10.1016/j.powtec.2003.08.017

Gouveia RF, Galembeck F (2009) Electrostatic charging of hydrophilic particles due to water adsorption. J Am Chem Soc 131:11381–11386. https://doi.org/10.1021/ja900704f

Grosshans H (2022) Verfahren zum Bestimmen zumindest eines Ladungskennwerts von elektrischen Ladungen von Partikeln in einem Fluidstrom und Fluidstromladungsmessgerät. Patent reference: 10 2021 101 409, 5 May 2022

Grosshans H, Jantač S (2023) Recent progress in CFD modeling of powder flow charging during pneumatic conveying. Chem Eng J 455:140918. https://doi.org/10.1016/j.cej.2022.140918

Grosshans H, Papalexandris MV (2017) Direct numerical simulation of triboelectric charging in particle-laden turbulent channel flows. J Fluid Mech 818:465–491. https://doi.org/10.1017/jfm.2017.157

Hammond A, Liang Z, Meng H (2019) Holographic deflection imaging measurement of electric charge on aerosol particles. Exp Fluids 40:103. https://doi.org/10.1007/s00348-019-2744-z

Jantac S, Grosshans H (2024) Suppression and control of bipolar powder charging by turbulence. Phys Rev Lett 132:054004. https://doi.org/10.1103/PhysRevLett.132.054004

Klinzing GE (2018) A review of pneumatic conveying status, advances and projections. Powder Technol 333:78–90. https://doi.org/10.1016/j.powtec.2018.04.012

Konopka L, Kosek J (2017) Discrete element modeling of electrostatic charging of polyethylene powder particles. J Electrostat 87:150–157. https://doi.org/10.1016/j.elstat.2017.04.008

Matsusaka S, Masuda H (2006) Simultaneous measurement of mass flow rate and charge-to-mass ratio of particles in gas–solids pipe flow. Chem Eng Sci 61(7):2254–2261. https://doi.org/10.1016/j.ces.2005.05.006

Mazumder M, Ware R, Yokoyama T et al (1991) Measurement of particle size and electrostatic charge distributions on toners using e-spart analyzer. IEEE Trans Ind Appl 27(4):611–619. https://doi.org/10.1109/28.85472

Mendez M, Raiola M, Masullo A et al (2017) POD-based background removal for particle image velocimetry. Exp Therm Fluid Sci 80:181–192. https://doi.org/10.1016/j.expthermflusci.2016.08.021

Ndama AT, Guigon P, Saleh K (2011) A reproducible test to characterise the triboelectric charging of powders during their pneumatic transport. J Electrostatics 69(3):146–156. https://doi.org/10.1016/j.elstat.2011.03.003

Peltonen J, Murtomaa M, Salonen J (2018) Measuring electrostatic charging of powders on-line during surface adhesion. J Electrostatics 93:53–57. https://doi.org/10.1016/j.elstat.2018.03.007

Savin T, Doyle PS (2005) Static and dynamic errors in particle tracking microrheology. Biophys J 88(1):623–638. https://doi.org/10.1529/biophysj.104.042457

Taghavivand M, Cho BJ, Mehrani P et al (2020) Electrostatic charging behaviour of a silica powder during pulse pneumatic conveying. Powder Technol 366:119–129. https://doi.org/10.1016/j.powtec.2020.02.031

Takahashi T (1973) Measurement of electric charge of cloud droplets, drizzle, and raindrops. Rev Geophys 11(4):903–924. https://doi.org/10.1029/RG011i004p00903

Toth JRI, Phillips AK, Rajupet S et al (2017) Particle-Size-Dependent Triboelectric Charging in Single-Component Granular Materials: Role of Humidity. Ind Eng Chem Res 56(35):9839–9845. https://doi.org/10.1021/acs.iecr.7b02328

Twomey S (1956) The electrification of individual cloud droplets. Tellus 8(4):445–452. https://doi.org/10.1111/j.2153-3490.1956.tb01247.x

van der Wel C, Kraft DJ (2017) Automated tracking of colloidal clusters with sub-pixel accuracy and precision. J Phys: Condens Matter 29(4):044001

Waitukaitis SR, Lee V, Pierson JM et al (2014) Size-dependent same-material tribocharging in insulating grains. Phys Rev Lett 112:218001. https://doi.org/10.1103/PhysRevLett.112.218001

Wells PV, Gerke RH (1919) An oscillation method for measuring the size of ultramicroscopic particles. JACS 41(3):312–329. https://doi.org/10.1021/ja01460a004

Xu W, Grosshans H (2023) Experimental study of humidity influence on triboelectric charging of particle-laden duct flows. J Loss Prev Process Ind 81:104970. https://doi.org/10.1016/j.jlp.2022.104970

Zhang H, Zhou YH (2020) Reconstructing the electrical structure of dust storms from locally observed electric field data. Nat Commun 11(1):5072. https://doi.org/10.1038/s41467-020-18759-0

Zhang H, Cui Y, Zheng X (2023) How electrostatic forces affect particle behaviour in turbulent channel flows. J Fluid Mech 967:A8. https://doi.org/10.1017/jfm.2023.459